A Slump in the Trench: Tracking the impact of the 2011 Tohoku-Oki earthquake

M.Strasser[1], M.Kölling[2], C. dos Santos Ferreira[2], H.G.Fink[2], T.Fujiwara[3], S.Henkel[4], K.Ikehara[5], T.Kanamatsu[3], K.Kawamura[6] , S.Kodaira[3], M.Römer[2], G.Wefer[2] and the R/V Sonne Cruise SO219A and JAMSTEC Cruise MR12-E01 scientists[7]

[1]Geological Institute, ETH Zurich, Sonneggstrasse 5, 8092 Zürich, Switzerland.

[2]MARUM – Center for Marine Environmental Sciences, University of Bremen, Leobener Strasse, 28359 Bremen Germany.

[3]Japan Agency of Marine Science and Technology (JAMSTEC), 2-15 Natsushima-Cho, Yokosuka-city, Kanagawa 237-0061, Japan.

[4] Geological Institute, University of Cologne, Zülpicherstrasse 49a, 50674 Köln, Germany.

[5]Geological Survey of Japan, National Institute of Advanced Industrial Science and Technology (AIST), Tsukaba, Ibaraki 305-8568, Japan.

[6]Departement of Geosphere Science, Yamaguchi University, Yamaguchi City, Yamaguchi 753-8512 Japan.

[7]Group authors (footnote).

ABSTRACT

We present differential bathymetry and sediment core data from the Japan Trench, sampled after the 2011 Tohoku-Oki earthquake to document that prominent bathymetric and structural changes along the trench axis relate to a large (~27.7 km^2) slump in the trench. Transient geochemical signals in the slump deposit and analyzing diffusive re-equilibration of disturbed

Footnote: Supplemental (Methods, Tables DR1-DR4, Figures DR1-DR3, author contribution) information is available online as GSA Data repository item XXX at http://www.geosociety.org/pubs/XXX.htm

SO_4^{2-} profiles over time, constrain that the slump was triggered by the 2011 earthquake. We propose a causal link between earthquake slip to the trench and rotational slumping above a subducting horst structure. We conclude that the earthquake-triggered slump is a leading agent for accretion of trench sediments into the forearc and hypothesize that forward growth of the prism and seaward advance of the deformation front by more than 2 km can occur, punctuated, during a single-event large mega-thrust earthquake.

INTRODUCTION

A striking feature common in various datasets collected during and after the 2011 Tohoku-Oki earthquake in the Japan Trench subduction zone is the evidence for co-seismic rupture propagation to a shallow depth near the trench (Ide et al., 2011; Ozawa et al., 2011; Yokota et al., 2011; Ito et al., 2011; Fujiwara et al., 2011; Kodaira et al., 2012). This shallow slip along the plate boundary fault resulted in co-seismic horizontal displacement of the seafloor, >50 m towards the East (Fujiwara et al., 2011; Ito et al., 2011), and significantly contributed to the generation of the destructive tsunami (Yokota et al., 2011). Additionally, large submarine landslides on the landward slope of the trench have been proposed as a new scenario for additional or amplification of tsunami (Kawamura et al., 2012). A submarine landslide as consequence of the 2011 earthquake has also been inferred from anomalies in differential bathymetry data documenting +/-50 m upward and downward changes in seafloor elevation along the lowermost landward slope of the trench and the trench axis, respectively (Fujiwara et al., 2011; here referred to as hypothesis 1). The positive anomaly, in contrast, has alternatively been interpreted as compressional structure (i.e. thrust-up structure) created by co-seismic slip breaking the seafloor at the trench (Kodaira et al., 2012; here referred to as hypothesis 2).

Footnote: Supplemental (Methods, Tables DR1-DR4, Figures DR1-DR3, author contribution) information is available online as GSA Data repository item XXX at http://www.geosociety.org/pubs/XXX.htm

Studies carried out in other subduction zones support the hypothesis of co-seismic fault slip potentially reaching close to the trench (Gulick et al., 2011; Henstock et al., 2006; Sakaguchi et al., 2011). Likewise, submarine landslides, presumably triggered by mega-thrust earthquakes, have been identified in marine-geophysical data along convergent margins worldwide (McAdoo et al., 2004; Ratzov et al., 2010). Landslides have also been proposed as agents in shaping the surface and controlling the stability of frontal prisms in such settings (Ratzov et al., 2010; von Huene et al., 2004). Such studies, however, often lack samples from the seafloor and subseafloor to groundtruth geophysical interpretation and models. Where cores are available, one of the remaining challenges is to adequately date recent deformation structures, in order to causally assign them to well-known very recent earthquakes. Only these data combined with geophysical data can allow discussion of the dynamic contribution of earthquakes and submarine landslides in shaping convergent margins on geologic vs. human timescales.

In this study, we present new data from two rapid-response cruises by the Japanese vessel *R/V Mirai* and the German vessel *R/V Sonne* (cruises MR12-E01 and SO-219A, respectively), which cored at the Japan Trench, 140 km seaward of the 2011 Tohoku-Oki earthquake epicenter in water depths up to 7.6 km (Fig 1). We use sediment core and pore-water geochemistry data to identify and date recent sediment remobilization processes. Several previous studies suggested that submarine landslides can impact the shape of pore-water profiles (Henkel et al., 2011; Hensen et al., 2003; Völker et al., 2011; Zabel, 2001). Generally, pore-water systems of deep-marine sediments in steady state are in equilibrium and show a linear SO_4^{2-} decrease with depth towards the sulfate-methane transition zone (Barnes and Goldberg, 1976). Drastic changes in sedimentation rate, CH_4 fluxes, intensity of bioirrigation, advective processes or, in particular, sediment disturbance during submarine landslides disrupt the steady state conditions (Henkel et al., 2011; Hensen et al., 2003). This disruption

Footnote: Supplemental (Methods, Tables DR1-DR4, Figures DR1-DR3, author contribution) information is available online as GSA Data repository item XXX at http://www.geosociety.org/pubs/XXX.htm

can lead to transient, kink-shape SO_4^{2-} profiles, which evolve into a concave and linear shape with time after the disturbance "event", due to molecular diffusion. Modeling the diffusive re-equilibration of SO_4^{2-} profiles thus allows for constraining the age of very young events, which disturbed the pore-water profiles (Henkel et al., 2011).

MULTIPLE LINES OF EVIDENCE FOR A SLUMP IN THE JAPAN TRENCH

Multibeam bathymetry and reflection seismic data

Our study focuses on a confined area immediately north of 38°N, along a W-E transect across the trench, where differential bathymetry (Fujiwara et al., 2011) and seismic data (Kodaira et al., 2012) revealed the most prominent changes between the 1999/2004 and 2011 datasets (Fig 1), presumed to be generated during the 2011 earthquake. There, the anomalies in differential bathymetry were hypothesized to reflect (1) a landslide (Fujiwara et al., 2011) or (2) co-seismic displacement induced thrusting in the trench axis (Kodaira et al., 2012). Our new bathymetry data collected during cruise SO219A extend the coverage of high-resolution post-2011 data along-strike, revealing upward-convex, horizontally-arcuate topographic features along the lowermost landward slope of the trench and parallel to the western boundary of the area with negative differential bathymetry values (Fig 1). Likewise, a trench-parallel ridge, up to 50 m above the trench floor, extends ~13km in a N-S direction, matching the area with positive differential bathymetry values. Correlative and well-defined northern and southern terminations of both structures suggest that they are causally linked. In total, we map an area of ~7.6 and 20.1 km^2 with average mean values of about -46m and +33m, for the negative and positive differential topographic elevation changes, respectively (Table DR1[footnote]). The area of bathymetric changes is spatially confined to a relatively narrow part (13 km along-strike) of the Japan Trench.

Footnote: Supplemental (Methods, Tables DR1-DR4, Figures DR1-DR3, author contribution) information is available online as GSA Data repository item XXX at http://www.geosociety.org/pubs/XXX.htm

Sediment core data

Sediment cores were retrieved and analyzed to (i) test the seemingly competing hypotheses 1 and 2 (i.e. the landslide and co-seismic displacement induced thrusting hypothesis by Fujiwara et al. (2011) and Kodaira et al. (2012), respectively) and (ii) to date the formation of the respective structures. The sedimentary succession in cores from the area with positive differential bathymetry anomaly (cores PC01, PC03, and PC05) is undisturbed and individual distinct layers stratigraphically correlate to respective layers in the succession of the trench fill (cores PC04, PC06, GeoB16433-1; Fig 2). This finding indicates that the positive differential bathymetry anomaly is not related to the deposition of sediment debris from recent landslides as proposed in the landslide hypothesis 1 by Fujiwara et al. (2011).

Similarly, both the core upslope (GeoB16425-1) and the core within the area of negative differential bathymetry anomaly (GeoB16427-1) reveal generally undisturbed stratigraphic successions, although beds are tilted up to 30° in GeoB16427-1, exceeding typical slope angles at this site (10-15°). Shear strength values measured in core GeoB16427-1 show an undisturbed linear trend with 2.3 kPa near the seafloor and 35-40 kPa 8 meter below seafloor (mbsf), indicating normally consolidated sediments (Table DR2, Figure DR1 [footnote]). Similarly, SO_4^{2-} values indicate steady state condition with values close to bottom water composition in the shallow most subsurface (27.95 mmol/l) and a linear decrease to 5 mmol/l in 8 mbsf, (Table DR3, Fig DR1[footnote]). These results clearly document that this site was not affected by 50m of sediment removal from submarine landslide in the recent past, as implied by hypothesis 1. Therefore, we conclude that the negative differential bathymetry anomaly results from subsidence rather than sediment removal. Together with our structural interpretation of the seafloor topography (Fig 1) and the observation of tilted beds indicating rotation of the strata, we infer a rotational slump mechanism.

Footnote: Supplemental (Methods, Tables DR1-DR4, Figures DR1-DR3, author contribution) information is available online as GSA Data repository item XXX at http://www.geosociety.org/pubs/XXX.htm

This interpretation is reinforced by clear evidence for slump deposits observed in cores GeoB16426-1 and -29-1, at the foot of the landward slope of the trench (Fig 2). These deposits are dominated by individual mud blocks, separated by dipping shear surfaces indicating material, which was not fully disaggregated, but rather experienced “ductile-type” deformation, typical for submarine slumps. Mud clasts floating in disintegrated matrix were only observed in the uppermost meter of core GeoB16429-1, whereas the top 23 cm of core GeoB16426-1 is characterized by massive-to-graded mud. We interpret these two uppermost facies as debrite and muddy low-density turbidites, respectively, evolving by water entrainment in the top of the slump and possibly also from seismo-turbidites deposited in the deepest depression of the trench.

DATING, OR HOW CAN WE TRACK THE IMPACT OF THE 2011 TOHOKU-OKI EARTHQUAKE?

Constantly-high unsupported ^{210}Pb activity (>1200 Bq/kg) measured within the deposit (Table DR4, Fig DR2[footnote]) reveals a geologically very young age of < 110 years (i.e. younger than 5 times the radioactive ^{210}Pb half-life = 22.3 yr (Noller, 2000)). Pore-water data from the two MTD-cores (Table DR3 [footnote]) clearly show distinct kink-shape depth profiles for SO_4^{2-} (Fig 3) as well as for a series of other geochemical species including Alkalinity and Ammonium (Table DR3, Fig DR1[footnote]). In this study, we focus on SO_4^{2-} values, for which the sharp kink is observed at correlative depths where we interpreted sediment-seawater mixing from visual core description. The kink confirms that we have captured a transient pore-water signal documenting a recent mixing with seawater, which is not yet completely re-equilibrated by molecular diffusion. To constrain the age of the disturbance event that caused the kink-shape SO_4^{2-} profile, we model diffusive transport of SO_4^{2-} using a numerical solution of Fick’s second law (Schulz and Schulz, 2005) [footnote]. Our simulation shows that the transient

Footnote: Supplemental (Methods, Tables DR1-DR4, Figures DR1-DR3, author contribution) information is available online as GSA Data repository item XXX at http://www.geosociety.org/pubs/XXX.htm

signal would be mostly equilibrated after only 10 years. Measured SO_4^{2-} data best fit sampling 0.5 to 2 years after the disturbance event (Fig. 3). Since the two cores were retrieved in March 2012, this result yields strong evidence that it was the March 2011 Tohoku-Oki earthquake (or one of its aftershocks) that triggered the observed slump, sediment remobilization and resulting disturbance of the pore-water profiles.

DISCUSSION AND IMPLICATIONS FOR THE EVOLUTION OF THE SHALLOW PLATE BOUNDARY SYSTEM

Our examination of the observed bathymetric structures and core data, combined with interpretation of seismic lines by Kodaira et al.(2012), leads us to hypothesis that a deep-seated rotational slump mechanism generated the observed features (Fig. 4). The detachment surface presumably soles into the décollement, where basal friction was dynamically reduced during co-seismic rupture (Kawamura et al., 2012). Additionally, there is a particular geometric situation of a subducting horst structure in the oceanic basement, the seaward edge of which is located just below the tip of the frontal prism (Kodaira et al., 2012). There, co-seismic displacement, with presumably high seismic horizontal ground accelerations, brought the sedimentary block over the graben, further favoring gravitational instability and slumping. The frontal part of such a frontally-confined rotational slump is in a state of compression, which typically results in frontal thrusting and bulging (Farrell, 1984; Frey-Martinez et al., 2006). Thus, the positive anomaly in differential bathymetry is likely to be genetically linked to the slump, as corroborated by our structural mapping showing that it is spatially confined to the subsiding head-region of the slump (Fig 1).

Compression at the toe of the frontally-confined rotational slump is difficult to be distinguished from compression induced by co-seismic rupture to the trench (Kodaira et al., 2012). Therefore, our proposed scenario, does not exclude co-seismic slip propagation to the

Footnote: Supplemental (Methods, Tables DR1-DR4, Figures DR1-DR3, author contribution) information is available online as GSA Data repository item XXX at http://www.geosociety.org/pubs/XXX.htm

trench as additional element of contractional strain in the trench sediment. To further determine the proportion of earthquake slip vs. slump-toe-thrusting for contractional strain in the trench sediment, we estimate sediment volumes from the negative and positive differential bathymetry (i.e. 0.35 and 0.66 km^3; Table DR1 [footnote]). Assuming a simple mass-balance scenario, these volumes suggest that the contribution of the slump is at least 53%. Therefore, our results lead us to conclude that the earthquake-triggered slump is the leading agent for the initiation of the small-scale (2-3 km in width, ~13 along strike), emergent submarine fold-and-thrust belt.

The dimensions of seafloor deformation, compared to (i) the shallow near-trench earthquake rupture area and (ii) the water depth of >7 km, is relatively small. Thus, our proposed mechanism did not contribute significantly to tsunami generation. A more striking result, however, is that the deformation front of the prism advances seaward by 2-3 km. This finding has implications for assessing the rate of structural evolution processes; on geological time scales, the Japan Trench is considered an erosive margin (Von Huene and Culotta, 1989). Our study, however, implies that significant accretion of trench sediment into the forearc can occur during a single-event large mega-thrust earthquake with shallow rupture and accompanied slumps in the trench. In particular, we hypothesize that this process is likely accentuated in a setting, where subducting high-relief (such as a seamount or, as in the case of our study area, a horst structure, the seaward edge of which below the frontal prism is critical to the mechanism driving slump initiation) has recently disturbed the frontal prism. Dynamic restoration of the prism to equilibrium conditions, as proposed in generic models (von Huene et al., 2004), occurs very fast relative to tectonic geological timescale (e.g. the formation of a 7.5 km-wide prism off Costa Rica in only 140 kyrs. (von Huene et al., 2004)). Our study now shows that, in fact, a forward growth of the prism and seaward advance of the deformation front by more than 2 km can occur, punctuated, within one single event during a period of

Footnote: Supplemental (Methods, Tables DR1-DR4, Figures DR1-DR3, author contribution) information is available online as GSA Data repository item XXX at http://www.geosociety.org/pubs/XXX.htm

seconds to minutes. Additionally, the creation of seafloor topography in the trench axis will affect trench sedimentation patterns, which in turn and on geologic timescales, may have further implications for the evolution of the trench and shallow most part of the seismogenic plate boundary system.

APPENDIX

[footnote] GSA Data Repository item XXX provides supplemental information on methods, data and author contribution and is available online at www.geosociety.org/pubs/XXX.htm, or on request from editing@geosociety.org or Documents Secretary, GSA, P.O. Box 9140, Boulder, CO 80301, USA.

ACKNOWLEDGMENTS

SO219A cruise was funded by the Federal Ministry of Education and Research of Germany (BMBF) and through Deutsche Forschungsgemeinschaft DFG. We acknowledge Dr. K. Mochizuki, Univ. Tokyo, for Japanese coordination of this cruise. MR12-E01 cruise was supported by the Ministry of Education, Culture, Sports, Science and Technology (MEXT) and the Japan Agency for Marine-Earth Science and Technology (JAMSTEC). This study is also supported by Swiss National Science Foundation (grant Nr. PP00P2-133481 to M.S.). We further acknowledge Dr. S. Kastens and I. Stimac for their help in gamma spectrometry at AWI, Bremerhaven. Drs. L. McNeill, S. Gullick, and an anonymous reviewer are acknowledged for helpful comments improving an early version of this paper. The data reported here will be archived at the following databases: Pangaea (link-placeholder: www.pangaea.de)

REFERENCES CITED

Footnote: Supplemental (Methods, Tables DR1-DR4, Figures DR1-DR3, author contribution) information is available online as GSA Data repository item XXX at http://www.geosociety.org/pubs/XXX.htm

Barnes, R. O., and Goldberg, E. D., 1976, Methane production and consumption in anoxic marine sediments: Geology, v. 4, no. 5, p. 297-300.

Farrell, S. G., 1984, A dislocation model applied to slump structures, Ainsa Basin, South Central Pyrenees: Journal of Structural Geology, v. 6, no. 6, p. 727-736.

Frey-Martinez, J., Cartwright, J., and James, D., 2006, Frontally confined versus frontally emergent submarine landslides: A 3D seismic characterisation: Marine and Petroleum Geology, v. 23, no. 5, p. 585-604.

Fujiwara, T., Kodaira, S., No, T., Kaiho, Y., Takahashi, N., and Kaneda, Y., 2011, The 2011 Tohoku-Oki Earthquake: Displacement Reaching the Trench Axis: Science, v. 334, no. 6060, p. 1240.

Grasshoff, K., Erhardt, M., and Kremling, 1983, Methods of Seawater Analysis: Weinheim, Verlag Chemie, p. 108-113.

Gulick, S. P. S., Austin, J. A., McNeill, L. C., Bangs, N. L. B., Martin, K. M., Henstock, T. J., Bull, J. M., Dean, S., Djajadihardja, Y. S., and Permana, H., 2011, Updip rupture of the 2004 Sumatra earthquake extended by thick indurated sediments: Nature Geosci, v. 4, no. 7, p. 453-456.

Henkel, S., Strasser, M., Schwenk, T., Hanebuth, T. J. J., Hüsener, J., Arnold, G. L., Winkelmann, D., Formolo, M., Tomasini, J., Krastel, S., and Kasten, S., 2011, An interdisciplinary investigation of a recent submarine mass transport deposit at the continental margin off Uruguay: Geochem. Geophys. Geosyst., v. 12, no. 8, p. Q08009.

Hensen, C., Zabel, M., Pfeifer, K., Schwenk, T., Kasten, S., Riedinger, N., Schulz, H. D., and Boetius, A., 2003, Control of sulfate pore-water profiles by sedimentary events and the significance of anaerobic oxidation of methane for the burial of sulfur in marine sediments: Geochimica et Cosmochimica Acta, v. 67, no. 14, p. 2631-2647.

Footnote: Supplemental (Methods, Tables DR1-DR4, Figures DR1-DR3, author contribution) information is available online as GSA Data repository item XXX at http://www.geosociety.org/pubs/XXX.htm

Henstock, T. J., McNeill, L. C., and Tappin, D. R., 2006, Seafloor morphology of the Sumatran subduction zone: Surface rupture during megathrust earthquakes?: Geology, v. 34, no. 6, p. 485-488.

Ide, S., Baltay, A., and Beroza, G. C., 2011, Shallow Dynamic Overshoot and Energetic Deep Rupture in the 2011 Mw 9.0 Tohoku-Oki Earthquake: Science, v. 332, no. 6036, p. 1426-1429.

Ito, Y., Tsuji, T., Osada, Y., Kido, M., Inazu, D., Hayashi, Y., Tsushima, H., Hino, R., and Fujimoto, H., 2011, Frontal wedge deformation near the source region of the 2011 Tohoku-Oki earthquake: Geophys. Res. Lett., v. 38, no. 15, p. L00G05.

Kawamura, K., Sasaki, T., Kanamatsu, T., Sakaguchi, A., and Ogawa, Y., 2012, Large submarine landslides in the Japan Trench: A new scenario for additional tsunami generation: Geophys. Res. Lett., v. 39, no. 5, p. L05308.

Kido, Y., Fujiwara, T., Sasaki, T., Kinoshita, M., Kodaira, S., Sano, M., Y., I., Hanafusa, Y., and Tsuboi, S., Bathymetric feature around Japan Trench obtained by JAMSTEC multi narrow beam survey,, *in* Proceedings Japan Geoscience Union Meeting 2011, Chiba, Japan, 2011 p. Paper No MIS036-P058.

Kodaira, S., No, T., Nakamura, Y., Fujiwara, T., Kaiho, Y., Takahashi, N., Kaneda, Y., and Taira, A., 2012, Coseismic fault rupture at the trench axis during the 2011 Tohoku-oki earthquake: Nature Geoscience, v. 5, p. 646-650.

McAdoo, B. G., Capone, M. K., and Minder, J., 2004, Seafloor geomorphology of convergent margins: Implications for Cascadia seismic hazard: Tectonics, v. 23, no. 6.

Noller, J. S., 2000, Lead-210 geochronology, Quaternary Geochronology: Methods and Applications, Volume 4: Washington, DC, AGU, p. 115-120.

Footnote: Supplemental (Methods, Tables DR1-DR4, Figures DR1-DR3, author contribution) information is available online as GSA Data repository item XXX at http://www.geosociety.org/pubs/XXX.htm

Ozawa, S., Nishimura, T., Suito, H., Kobayashi, T., Tobita, M., and Imakiire, T., 2011, Coseismic and postseismic slip of the 2011 magnitude-9 Tohoku-Oki earthquake: Nature, v. 475, no. 7356, p. 373-376.

Ratzov, G., Collot, J.-Y., Sosson, M., and Migeon, S., 2010, Mass-transport deposits in the northern Ecuador subduction trench: Result of frontal erosion over multiple seismic cycles: Earth and Planetary Science Letters, v. 296, no. 1-2, p. 89-102.

Sakaguchi, A., Chester, F., Curewitz, D., Fabbri, O., Goldsby, D., Kimura, G., Li, C.-F., Masaki, Y., Screaton, E. J., Tsutsumi, A., Ujiie, K., and Yamaguchi, A., 2011, Seismic slip propagation to the updip end of plate boundary subduction interface faults: Vitrinite reflectance geothermometry on Integrated Ocean Drilling Program NanTroSEIZE cores: Geology.

Schulz, H. N., and Schulz, H. D., 2005, Large Sulfur Bacteria and the Formation of Phosphorite: Science, v. 307, no. 5708, p. 416-418.

Völker, D., Scholz, F., and Geersen, J., 2011, Analysis of submarine landsliding in the rupture area of the 27 February 2010 Maule earthquake, Central Chile: Marine Geology, v. 288, no. 1–4, p. 79-89.

Von Huene, R., and Culotta, R., 1989, Tectonic erosion at the front of the Japan Trench convergent margin: Tectonophysics, v. 160, no. 1–4, p. 75-90.

von Huene, R., Ranero, C. R., and Vannucchi, P., 2004, Generic model of subduction erosion: Geology, v. 32, no. 10, p. 913-916.

Yokota, Y., Koketsu, K., Fujii, Y., Satake, K., Sakai, S. i., Shinohara, M., and Kanazawa, T., 2011, Joint inversion of strong motion, teleseismic, geodetic, and tsunami datasets for the rupture process of the 2011 Tohoku earthquake: Geophys. Res. Lett., v. 38, p. L00G21.

Footnote: Supplemental (Methods, Tables DR1-DR4, Figures DR1-DR3, author contribution) information is available online as GSA Data repository item XXX at http://www.geosociety.org/pubs/XXX.htm

Zabel, M., 2001, Importance of submarine landslides for non-steady state conditions in pore water systems - lower Zaire (Congo) deep-sea fan: Marine Geology, v. 176, p. 87-99.

FIGURE CAPTIONS

Figure 1. Interpreted bathymetric map of the Japan Trench, 140 km seaward of the 2011 Tohoku-Oki earthquake epicenter (black star in inlet map): Background shaded relief and 20 m-contour lines represent post-2011 bathymetry. Color coding indicates relative changes in bathymetry from data acquired before and after the earthquake: Warm colored differential bathymetry (between dashed lines) is reproduced from Fujiwara et al. (2011), and based on comparison of high-resolution bathymetry data acquired in 1999 and 2011. Diminished color hues north and south show the pre-to-post earthquake bathymetry differences by comparing lower-resolution 90 m bathymetry model (Kido et al., 2011) with new data acquired during *SO219A* (this study). Core locations of *SO219A* and *MR12-E01* are given in green and yellow, respectively.

Figure 2. Transect showing post-earthquake bathymetric profile and lithological logs of cores GeoB16425-1, -27-1, -29-1, -26-1,and cores PC05 and PC06 acquired during SO219A and MR12-E01, respectively. V.E. = vertical exaggeration. The relative core depth scale is 20x vertically exaggerated with respect to the bathymetric profile. For legend of symbols used see Fig DR1[footnote].

Figure 3. Geochemical pore-water profiles and diffusive re-equilibration calculations: A) and B); Measured SO_4^{2-} concentrations (discrete data points) and modeled profiles according to the diffusive re-equilibration after initial disturbance, for the upper parts of cores GeoB16426-

Footnote: Supplemental (Methods, Tables DR1-DR4, Figures DR1-DR3, author contribution) information is available online as GSA Data repository item XXX at http://www.geosociety.org/pubs/XXX.htm

1 and -29-1, respectively. Equilibrium conditions are predicted to be reached within 10 years, and measured SO_4^{2-} data best fit sampling 0.5 to 2 years after the disturbance event.

Figure 4:

Conceptual sketch integrating interpretation of seismic data by Kodaira et al. (2012) before (A) and after (B) the earthquake and results from analysis of new bathymetric and core data from SO219A and MR12-E01: We propose a causal link between 1) earthquake rupture to the trench, (2) rotational slumping induced by co-seismic displacement of the sedimentary block above the horst structure over the graben, and (3) compressional effects resulting in forward imbrication and accretion of trench material into a 2-3 km-wide emerging submarine fold-and-thrust belt. The deformation front advances seaward by 2-3km, establishing a new frontal thrust/décollement system in the Japan Trench after the earthquake.

Footnote: Supplemental (Methods, Tables DR1-DR4, Figures DR1-DR3, author contribution) information is available online as GSA Data repository item XXX at http://www.geosociety.org/pubs/XXX.htm

Figure 1
Click here to download Figure: Fig1_map.pdf

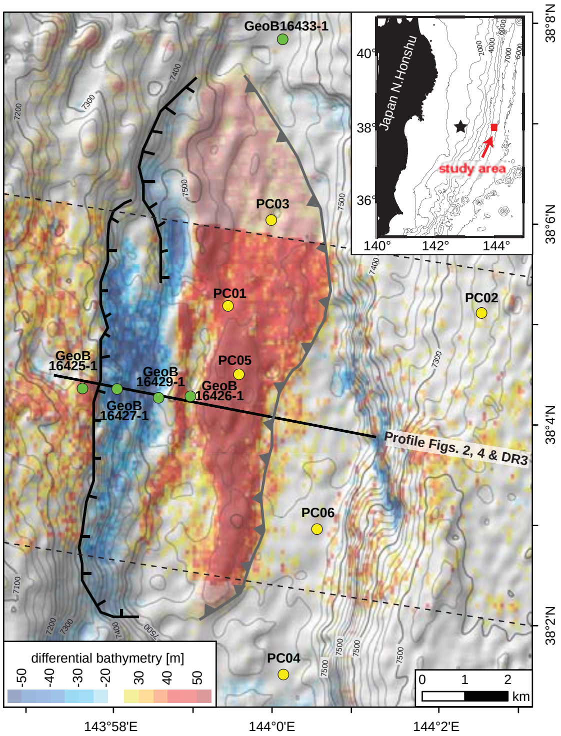

Fig 1:

Figure 2
Click here to download Figure: Fig2_Trenchprofile with cores.pdf

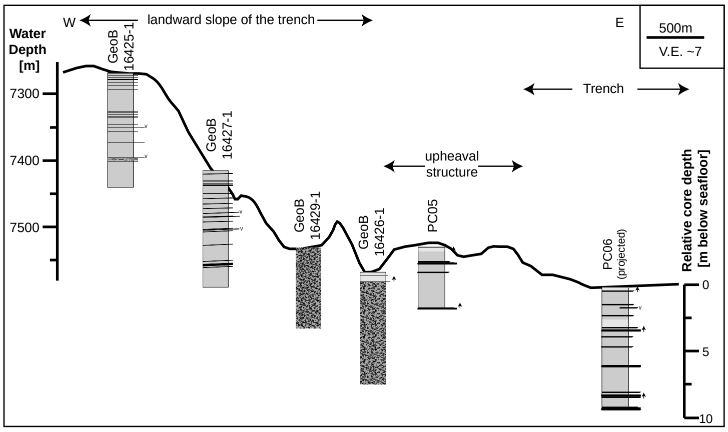

Figure 2.

Figure 3
Click here to download Figure: Fig3_Pore-water-Geochemistry.pdf

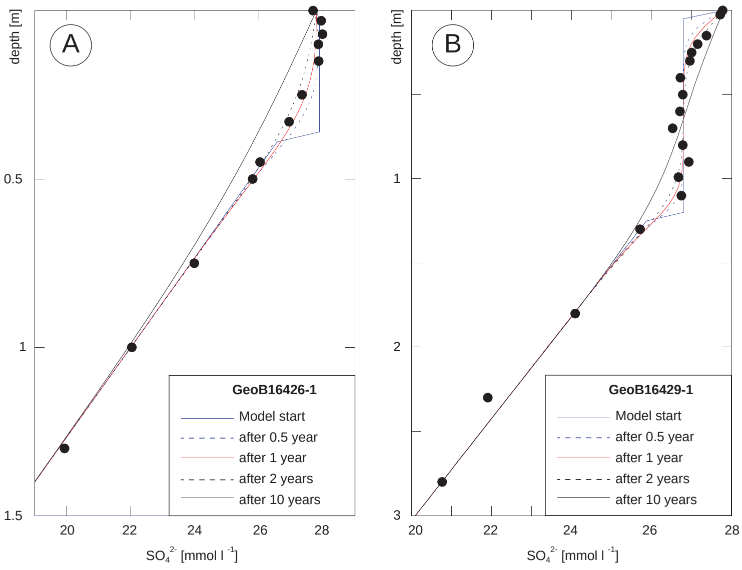

Figure 3:

Figure 4

Click here to download Figure: Fig4_interpretativ-sketch.pdf

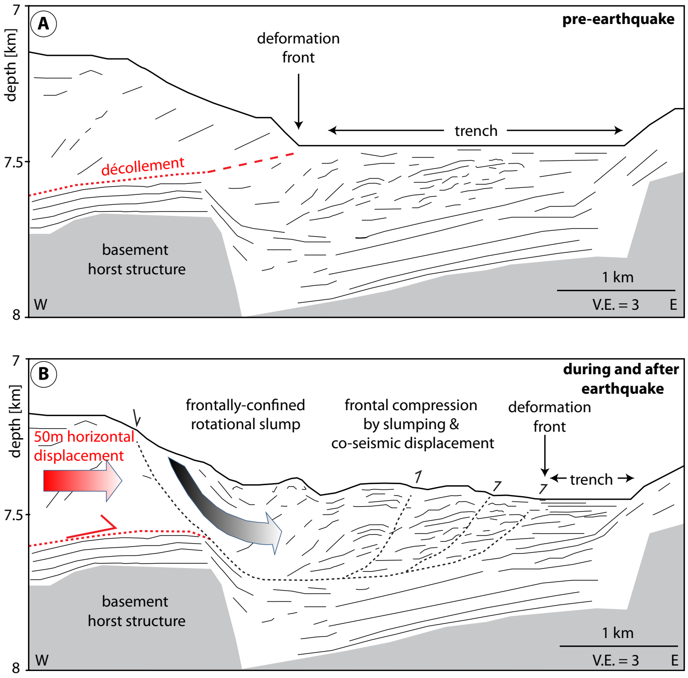

Figure 4

Data Repository item Strasser et al.,

MATERIAL AND METHODS

Multibeam bathymetry data

Bathymetric data during *R/V Sonne* Cruise *SO219A* were acquired at a survey speed of mostly 6 knots (4 knots for selected detailed mapping surveys), using a *KONGSBERG* EM 120 multibeam echosounder operated at 12 kHz. The transducers have a nominal opening of 2° in along-track direction and also 2° in across track direction. The multibeam echosounder is capable of recording up to 191 individual beams across track within a swath of up to 150°. However, for the purpose of detailed bathymetry mapping in the study area, the swath width was reduced to 90°. For analysis (Fig 1), we only use the data obtained by beams within a 45° swath width, because these inner beam soundings have higher accuracy and fewer artifacts caused by errors in water column sound velocity. With this unified set-up, *SO219A* data are directly comparable with the data by Fujiwara et al.(2011) and we stringently followed their approach in processing, gridding and calculating differential data comparing pre- and post-2011 bathymetry.

Spatial statistical analyses of the prominent negative and positive anomalies identified and mapped in the differential data set were performed using the “zonal statistics tool” implemented in the GIS software package ArcGis. From his data, “subsided” and “bulged” sediment volumes in the headwall and toe region are estimated by multiplying mean values and area of the negative and positive anomalies, respectively. Results are presented in table DR1.

Seismic Data

Our interpretation of the subsurface and the conceptual model for slumping and bulging shown in Figure 4 is based on interpretations of seismic lines published by Kodaira et al. (2012; their figure 4a, 4b and S4a). For information, we show these seismic lines reproduced from Kodaira et al. (2012) in Figure S3. As already mentioned by Kodaira et al., (2012), one cannot exclude that deformed structures in the subsurface without positive seafloor expression in the trench were present before the 2011-event and may partly have resulted from cumulative effect of past slip-to-the-trench earthquakes, because there are no high resolution pre-2011 seismic data available. However, structural mapping of our new bathymetry data north and south of the transect studied by Fujiwara et al. (2011) and Kodaira et al. (2012) as shown in Figure 1 corroborates our interpretation that the upheaval structure and thus the up-thrusting of trench material is genetically linked to the slump.

Core sampling

Sediment cores were retrieved using a gravity corer and piston coring system operated onboard *R/V Sonne* and *R/V Mirai*, respectively. Closed *SO219A* gravity cores were sampled for interstitial water close to *in situ* sediment temperature within the first three hours after retrieval, using rhizon samplers (Seeberg-Elverfeldt et al., 2005). The sampling interval was generally 3 cm (0 to 15 cm), 5 cm (15 to 30 cm), 10 cm (30 to 100 cm) 25 cm (100 to 200 cm) and 50 cm (below 200 cm). Based on the first results, additional samples were taken from the working core half of all three cores presented in this study to increase the resolution of the data. The pore-water flow was generally good, so that most sample volumes were between 5 and 18 ml after a maximum of three hours. For the determination of the ^{210}Pb activity, sediment samples from the uppermost 78 cm of core GeoB16426-1 were taken every 5-10 cm using 10 ml plastic syringes with cut tips.

Physical property and sedimentological analysis:

The undrained shear strength of the sediment was determined on the working half every 10-15 cm using a Wykeham-Farrance cone penetrometer WF 21600 and following the procedures after Wood (Wood, 1985). Bulk density and fractional porosity, which were also used as input parameters for modeling of the sulfate profile development (see below section 1.5) and for processing gamma spectrometry data (see below section 1.6) were measured on a *Geotek* Multi Sensor Core Logger at Bremen Core Repository, MARUM (University of Bremen), and data were processed following the procedure after Blum (1997).

Sedimentological investigations involved a detailed visual core description and analysis of smear slides under a cross-polarizing microscope.

Pore-water analysis

Alkalinity was determined onboard *R/V Sonne* by pH controlled titration with HCl. The algorithm used to calculate alkalinity is modified after (Grasshoff et al., 1983) and accounts for the activity of seawater and dilution by the titration solution so that the results are stable for different endpoint pH values (see http://www.marum.de/en/Alkalinity_pH.html). The measurement has an accuracy of better than 0.2 mmol/l.

Ammonium was detected onboard *R/V Sonne* using the PTFE tape gas separator technique (modified after Hall and Aller (1992)). The detection limit is 5 µM, and accuracy is better than 1 %.

Sulfate concentrations were determined by means of ion chromatography (Metrohm IC Advanced Compact 861) with an analytical error <3 %.

Diffusion modeling of the pore-water sulfate profile

The re-equilibration of the kink shape SO_4^{2-} profile in the upper parts of sites GeoB164-26 and -29, based on molecular diffusion was simulated with the spreadsheet model *EXPLICIT* (Schulz and Schulz, 2005). Diffusive transport of SO_4^{2-} [diffusion coefficient in sediment D_{sed} = 3.34 E-10 m^2/s at 5°C, with a porosity of 0.7, as measured in the cores (Fig DR1), and tortuosity of 1.31] was calculated for a one-dimensional column using explicit numerical solution of Fick's law of diffusion (Schulz and Schulz, 2005). Initial boundary conditions were derived assuming steady state linear profiles below and initially fully mixed conditions immediately after the "initial disturbance event" above the observed sedimentary contacts.

Non-destructive gamma spectrometry

Analyses of ^{210}Pb and ^{226}Ra were performed at the Alfred-Wegener-Institute for Polar and Marine Research in Bremerhaven. The sediment samples were freeze-dried and ground in an agate mortar. About 6-7 g of the pulverized sediments were closed airtight in petri dishes and stored for 1 month. These samples were subsequently analyzed by nondestructive gamma spectrometry using a Canberra Broad Energy GE-Detector. Sample analyses ran for a minimum of 48h each. Unsupported ^{210}Pb ($^{210}Pb_{unsupp}$; airborne, not produced in the sediment by decay of ^{226}Ra) was calculated for each depth by subtracting the supported ^{210}Pb that is based on ^{226}Ra ($^{210}Pb_{supp}$) from the measured total activity of ^{210}Pb in the sample.

SUPPLEMENTARY TABLES AND FIGURES

Table DR1: Results from zonal statistical analysis of mapped areas showing positive and negative differential bathymetry anomalies.

Table DR2: Undrained shear strength from cone penetration testing

Table DR3: Interstitial pore water geochemistry data

Table DR4: Results from nondestructive gamma spectrometry measuring total, supported and unsupported 210Pb activity at site GeoB16426-1

Figure DR1: Physical property and pore-water geochemistry data of cores GeoB16426-1, -27-1 and -29-1:

Figure DR2: Results from nondestructive gamma spectrometry showing total, supported and unsupported ^{210}Pb activity measured for the uppermost 80 cm at site GeoB16426-1. Error bars of analytical measurements are smaller than the symbol size.

Figure DR3: Comparison of seismic images obtained before and after the earthquake, reproduced from Kodaira et al., (2012; Their figure 4a, 4b and S4a). A. Seismic image of the trench axis obtained in 1999 before the earthquake. An interface imaged ~200 m below the seafloor (black interface) at the landward slope of the trench is an artifact generated by a bubble signal from a non-tuned large airgun. Vertical exaggeration, 2:1. B Seismic image of the trench axis obtained after the earthquake. Vertical exaggeration, 2:1. C. High-resolution seismic image obtained after the earthquake around the trench (within the rectangle shown in Fig S3b)

Table DR1: Results from zonal statistical analysis of mapped areas showing positive and negative differential bathymetry anomalies.

feature in differential bathymetry set	area [m^2]	area [km^2]	mean elevation change [m]	Sediment volume [km]	Relative proportion [ ] by area	Relative proportion [ ] by volume
negative anomaly on landward slope of the trench	7671438	7.67	46.23	0.35	0.38	0.53
positive anomaly in the trench	20117490	20.12	33.02	0.66	2.62	1.87

Table DR2: Undrained Shear Strength from Cone Penetration Testing

Core	Depth (mbsf)	shear strength (kPa)
GeoB16426-1	0.04	0.91
GeoB16426-1	0.14	0.91
GeoB16426-1	0.24	1.09
GeoB16426-1	0.34	1.79
GeoB16426-1	0.41	3.92
GeoB16426-1	0.48	2.85
GeoB16426-1	0.55	3.30
GeoB16426-1	0.62	4.40
GeoB16426-1	0.69	6.01
GeoB16426-1	0.76	13.55
GeoB16426-1	0.83	5.38
GeoB16426-1	0.9	6.96
GeoB16426-1	0.97	7.27
GeoB16426-1	1.04	5.83
GeoB16426-1	1.26	109.15
GeoB16426-1	1.33	5.76
GeoB16426-1	1.43	7.41
GeoB16426-1	1.53	7.02
GeoB16426-1	1.63	10.54
GeoB16426-1	1.73	7.47
GeoB16426-1	1.83	7.18
GeoB16426-1	1.93	10.98
GeoB16426-1	2.03	12.13
GeoB16426-1	2.13	16.34
GeoB16426-1	2.23	21.10
GeoB16426-1	2.33	10.39
GeoB16426-1	2.43	49.57
GeoB16426-1	2.53	17.87
GeoB16426-1	2.63	94.88
GeoB16426-1	2.73	80.94
GeoB16426-1	2.83	104.06
GeoB16426-1	2.93	79.28
GeoB16426-1	3.03	58.07
GeoB16426-1	3.13	15.27
GeoB16426-1	3.23	10.76
GeoB16426-1	3.33	8.27
GeoB16426-1	3.43	17.02
GeoB16426-1	3.53	17.52
GeoB16426-1	3.63	14.87
GeoB16426-1	3.73	34.36
GeoB16426-1	3.83	14.31
GeoB16426-1	3.93	43.91
GeoB16426-1	4.03	26.85
GeoB16426-1	4.13	16.60
GeoB16426-1	4.23	17.58
GeoB16426-1	4.33	15.23
GeoB16426-1	4.43	17.69
GeoB16426-1	4.53	28.42
GeoB16426-1	4.63	40.93
GeoB16426-1	4.73	45.53
GeoB16426-1	4.83	66.39
GeoB16426-1	4.93	26.85
GeoB16426-1	5.03	30.91
GeoB16426-1	5.13	8.27
GeoB16426-1	5.23	9.42
GeoB16426-1	5.33	16.29
GeoB16426-1	5.43	18.90
GeoB16426-1	5.53	41.96
GeoB16426-1	5.6	46.74
GeoB16426-1	5.63	32.86
GeoB16426-1	5.73	23.81
GeoB16426-1	5.83	31.05
GeoB16426-1	5.93	102.44
GeoB16426-1	6.03	77.67
GeoB16426-1	6.13	69.41
GeoB16426-1	6.23	41.96
GeoB16426-1	6.33	39.36
GeoB16426-1	6.43	29.38
GeoB16426-1	6.53	42.59
GeoB16426-1	6.63	70.77
GeoB16426-1	6.73	50.95
GeoB16426-1	6.83	83.23
GeoB16426-1	6.93	20.03
GeoB16426-1	7.03	43.69
GeoB16426-1	7.13	62.40
GeoB16426-1	7.23	32.43
GeoB16426-1	7.25	169.52
GeoB16426-1	7.33	23.99
GeoB16426-1	7.43	33.45
GeoB16426-1	7.53	18.40
GeoB16426-1	7.63	65.56
GeoB16426-1	7.73	86.24
GeoB16426-1	7.83	178.38
GeoB16426-1	7.93	102.44
GeoB16426-1	8.03	28.78
GeoB16426-1	8.13	17.02
GeoB16426-1	8.23	24.36

Core	Depth (mbsf)	shear strength (kPa)
GeoB16427-1	0.02	2.34
GeoB16427-1	0.12	6.92
GeoB16427-1	0.22	5.24
GeoB16427-1	0.32	7.95
GeoB16427-1	0.42	6.74
GeoB16427-1	0.52	9.65
GeoB16427-1	0.62	7.88
GeoB16427-1	0.72	10.89
GeoB16427-1	0.82	7.24
GeoB16427-1	0.92	8.81
GeoB16427-1	1.02	7.83
GeoB16427-1	1.12	9.38
GeoB16427-1	1.22	8.05
GeoB16427-1	1.32	7.44
GeoB16427-1	1.42	9.29
GeoB16427-1	1.52	8.81
GeoB16427-1	1.62	8.21
GeoB16427-1	1.72	8.73
GeoB16427-1	1.82	10.87
GeoB16427-1	1.92	11.56
GeoB16427-1	2.02	11.62
GeoB16427-1	2.12	15.60
GeoB16427-1	2.22	16.39
GeoB16427-1	2.32	17.58
GeoB16427-1	2.42	14.78
GeoB16427-1	2.52	15.84
GeoB16427-1	2.62	15.70
GeoB16427-1	2.72	17.19
GeoB16427-1	2.82	16.19
GeoB16427-1	2.92	14.65
GeoB16427-1	3.02	17.35
GeoB16427-1	3.12	18.52
GeoB16427-1	3.22	20.88
GeoB16427-1	3.32	20.38
GeoB16427-1	3.42	19.48
GeoB16427-1	3.52	18.52
GeoB16427-1	3.62	17.87
GeoB16427-1	3.72	16.04
GeoB16427-1	3.82	19.48
GeoB16427-1	3.92	28.42
GeoB16427-1	4.02	22.85
GeoB16427-1	4.12	24.64
GeoB16427-1	4.22	30.39
GeoB16427-1	4.32	23.72
GeoB16427-1	4.42	19.35
GeoB16427-1	4.52	23.81
GeoB16427-1	4.62	23.37
GeoB16427-1	4.72	30.26
GeoB16427-1	4.82	28.42
GeoB16427-1	4.92	28.08
GeoB16427-1	5.02	33.90
GeoB16427-1	5.12	32.86
GeoB16427-1	5.22	16.86
GeoB16427-1	5.32	19.96
GeoB16427-1	5.32	32.29
GeoB16427-1	5.42	19.03
GeoB16427-1	5.52	19.82
GeoB16427-1	5.54	8.18
GeoB16427-1	5.59	21.95
GeoB16427-1	5.62	22.77
GeoB16427-1	5.7	14.78
GeoB16427-1	5.72	12.06
GeoB16427-1	5.82	17.52
GeoB16427-1	5.92	18.22
GeoB16427-1	5.99	38.06
GeoB16427-1	6.02	85.63
GeoB16427-1	6.12	24.36
GeoB16427-1	6.22	23.37
GeoB16427-1	6.32	25.81
GeoB16427-1	6.42	32.86
GeoB16427-1	6.52	30.01
GeoB16427-1	6.62	27.40
GeoB16427-1	6.72	40.93
GeoB16427-1	6.82	19.75
GeoB16427-1	6.92	60.54
GeoB16427-1	7.02	25.21
GeoB16427-1	7.12	37.17
GeoB16427-1	7.22	29.26
GeoB16427-1	7.32	39.94
GeoB16427-1	7.42	34.21
GeoB16427-1	7.52	39.17
GeoB16427-1	7.62	38.79
GeoB16427-1	7.72	26.64
GeoB16427-1	7.82	35.81
GeoB16427-1	7.92	38.61
GeoB16427-1	8.02	38.61
GeoB16427-1	8.12	30.39
GeoB16427-1	822.00	38.98
GeoB16427-1	832.00	31.05
GeoB16427-1	842.00	56.73
GeoB16427-1	852.00	24.92

Core	strengh depth [cm]	c_u from cone [kPa]
GeoB16429-1	8.00	2.00
GeoB16429-1	18.00	13.06
GeoB16429-1	28.00	16.24
GeoB16429-1	38.00	15.51
GeoB16429-1	48.00	4.67
GeoB16429-1	58.00	16.86
GeoB16429-1	68.00	6.11
GeoB16429-1	78.00	2.85
GeoB16429-1	88.00	17.87
GeoB16429-1	98.00	24.54
GeoB16429-1	108.00	5.78
GeoB16429-1	118.00	9.74
GeoB16429-1	128.00	10.70
GeoB16429-1	138.00	16.34
GeoB16429-1	148.00	7.24
GeoB16429-1	158.00	14.31
GeoB16429-1	168.00	25.51
GeoB16429-1	178.00	16.24
GeoB16429-1	188.00	21.95
GeoB16429-1	198.00	17.02
GeoB16429-1	208.00	21.10
GeoB16429-1	218.00	18.22
GeoB16429-1	228.00	28.42
GeoB16429-1	238.00	22.77
GeoB16429-1	248.00	23.45
GeoB16429-1	258.00	38.24
GeoB16429-1	268.00	23.28
GeoB16429-1	278.00	33.45
GeoB16429-1	288.00	52.09
GeoB16429-1	298.00	30.52
GeoB16429-1	308.00	54.18
GeoB16429-1	318.00	65.15
GeoB16429-1	328.00	59.82
GeoB16429-1	338.00	41.13
GeoB16429-1	348.00	51.51
GeoB16429-1	358.00	56.40
GeoB16429-1	368.00	32.14
GeoB16429-1	378.00	41.34
GeoB16429-1	388.00	68.53
GeoB16429-1	398.00	159.75
GeoB16429-1	408.00	135.00
GeoB16429-1	413.00	137.45
GeoB16429-1	418.00	34.36
GeoB16429-1	428.00	64.75
GeoB16429-1	438.00	49.30
GeoB16429-1	448.00	31.86
GeoB16429-1	458.00	53.27
GeoB16429-1	468.00	103.24
GeoB16429-1	478.00	37.17
GeoB16429-1	488.00	34.05
GeoB16429-1	498.00	61.27
GeoB16429-1	508.00	35.81
GeoB16429-1	518.00	23.45
GeoB16429-1	528.00	32.57
GeoB16429-1	538.00	18.77
GeoB16429-1	548.00	74.59
GeoB16429-1	558.00	76.62
GeoB16429-1	568.00	88.77
GeoB16429-1	578.00	72.64
GeoB16429-1	588.00	100.86
GeoB16429-1	598.00	178.38

Table DR3: Interstitial Porewater Geochemistry Data

Core	Depth (mbsf)	Alkalinity (mmol/l	Ammonium (mmol/l)	Sulphate (mmol/l
GeoB16426-1	0.00	2.31	0.00	27.70
GeoB16426-1	0.03	4.12	0.09	27.96
GeoB16426-1	0.07	4.89	0.16	27.99
GeoB16426-1	0.10	5.22	0.17	27.86
GeoB16426-1	0.15	6.03	0.20	27.87
GeoB16426-1	0.25	5.80	0.16	27.35
GeoB16426-1	0.33	4.77	0.11	26.95
GeoB16426-1	0.45	5.71	0.13	26.04
GeoB16426-1	0.50	6.65	0.18	25.81
GeoB16426-1	0.75	8.01	0.29	23.99
GeoB16426-1	1.00	11.76	0.41	22.04
GeoB16426-1	1.30	15.33	0.56	19.93
GeoB16426-1	1.80	23.90	0.85	15.37
GeoB16426-1	2.30	26.24	1.15	12.59
GeoB16426-1	2.80	29.89	1.32	10.10
GeoB16426-1	3.30	32.63	1.38	7.96
GeoB16426-1	3.80	36.88	1.55	5.74
GeoB16426-1	4.30	39.49	1.61	4.35
GeoB16426-1	4.80	42.09	1.70	2.99
GeoB16426-1	5.30	46.71	1.84	1.35
GeoB16426-1	5.80	47.82	1.95	0.54
GeoB16426-1	6.30	48.98	2.10	0.04
GeoB16426-1	6.80	50.55	2.06	0.01
GeoB16426-1	7.30	52.63	2.23	
GeoB16426-1	7.80	51.77	2.55	0.01
GeoB16426-1	8.30	51.88	2.60	0.36
GeoB16426-1	8.39	48.11	2.50	2.61

Core	Depth (mbsf)	Alkalinity (mmol/l)	Ammonium (mmol/l)	Sulphate (mmol/l)
GeoB16427-1	0.00	2.26	0.00	27.95
GeoB16427-1	0.04	3.88	0.09	26.42
GeoB16427-1	0.07	3.97	0.11	26.71
GeoB16427-1	0.10	4.14	0.12	26.46
GeoB16427-1	0.13	4.23	0.11	26.43
GeoB16427-1	0.16	4.48	0.13	26.28
GeoB16427-1	0.20	4.65	0.15	26.14
GeoB16427-1	0.25	4.73	0.16	26.18
GeoB16427-1	0.30	5.02	0.18	25.90
GeoB16427-1	0.40	5.46	0.21	25.73
GeoB16427-1	0.50	5.82	0.25	25.40
GeoB16427-1	0.60	6.28	0.29	25.17
GeoB16427-1	0.70	6.98	0.34	24.72
GeoB16427-1	0.80	7.20	0.36	24.44
GeoB16427-1	0.90	7.60	0.38	24.10
GeoB16427-1	1.00	8.01	0.41	23.99
GeoB16427-1	1.20	9.01	0.50	23.19
GeoB16427-1	1.40	9.69	0.59	22.69
GeoB16427-1	1.60	10.50	0.61	21.96
GeoB16427-1	2.00	11.97	0.79	20.87
GeoB16427-1	2.50	14.65	0.88	19.56
GeoB16427-1	3.00	16.63	1.12	18.05
GeoB16427-1	3.50	18.52	1.24	16.51
GeoB16427-1	4.00	20.26	1.43	14.97
GeoB16427-1	4.50	21.70	1.56	13.33
GeoB16427-1	5.00	23.12	1.74	12.43
GeoB16427-1	5.50	24.90	1.92	11.29
GeoB16427-1	5.99	26.89		10.03
GeoB16427-1	6.00	27.15	2.09	10.03
GeoB16427-1	6.11	27.95		9.04
GeoB16427-1	6.50	29.83	2.29	8.72
GeoB16427-1	7.00	31.82	2.58	6.47
GeoB16427-1	7.50	33.06	2.72	5.64
GeoB16427-1	8.00	33.83	2.87	5.10
GeoB16427-1	8.50	34.82	3.03	4.48

Core	Depth (mbsf)	Alkalinity (mmol/l)	Ammonium (mmol/l)	Sulphate (mmol/l)
GeoB16429-1	0.00	2.29	0.00	27.78
GeoB16429-1	0.03	3.00	0.04	27.72
GeoB16429-1	0.15	3.84	0.11	27.38
GeoB16429-1	0.20	4.15		27.16
GeoB16429-1	0.25	4.17	0.16	27.00
GeoB16429-1	0.30	4.20		26.96
GeoB16429-1	0.35	4.28	0.19	28.05
GeoB16429-1	0.40	4.26		26.72
GeoB16429-1	0.50	4.45	0.18	26.78
GeoB16429-1	0.60	4.86	0.19	26.71
GeoB16429-1	0.70	4.45	0.16	26.53
GeoB16429-1	0.80	3.78	0.09	26.78
GeoB16429-1	0.90	3.45	0.05	26.94
GeoB16429-1	0.99	3.58	0.05	26.67
GeoB16429-1	1.10	3.96	0.11	26.75
GeoB16429-1	1.30	5.32	0.21	25.72
GeoB16429-1	1.80	7.37	0.32	24.10
GeoB16429-1	2.30	8.94	0.45	21.91
GeoB16429-1	2.80	10.65	0.53	20.77
GeoB16429-1	3.30	12.86	0.63	19.84
GeoB16429-1	3.80	13.48	0.68	19.03
GeoB16429-1	4.30	14.79	0.78	18.33
GeoB16429-1	4.80	15.85	0.87	17.63
GeoB16429-1	5.30	19.15	1.14	14.98
GeoB16429-1	5.80	20.73	1.28	13.61
GeoB16429-1	5.95	18.09	1.29	15.19

Table DR4: Results from nondestructive gamma spectrometry measuring total, supported and unsupported 210Pb activity at site GeoB16426-1

depth [cm]	210Pb total [Bq/kg]	error	210Pb supported [Bq/kg]	error	210Pb unsupported	error
3.00	1293.04	10.86	49.73	0.99	1253.85	10.99
8.00	1305.80	9.40	50.24	0.86	1267.61	9.53
13.00	1588.87	13.79	64.85	1.26	1539.83	13.99
23.00	1327.98	11.73	52.74	1.08	1289.24	11.91
33.00	60.90	3.15	54.04	1.03	6.94	3.35
48.00	54.18	2.71	52.76	0.90	1.43	2.89
58.00	41.28	1.91	52.58	0.65	-11.41	2.04
73.00	48.50	2.07	50.13	0.68	-1.65	2.20
78.00	62.09	1.87	65.23	0.64	-3.17	1.99

SUPPLEMENTARY FIGURES

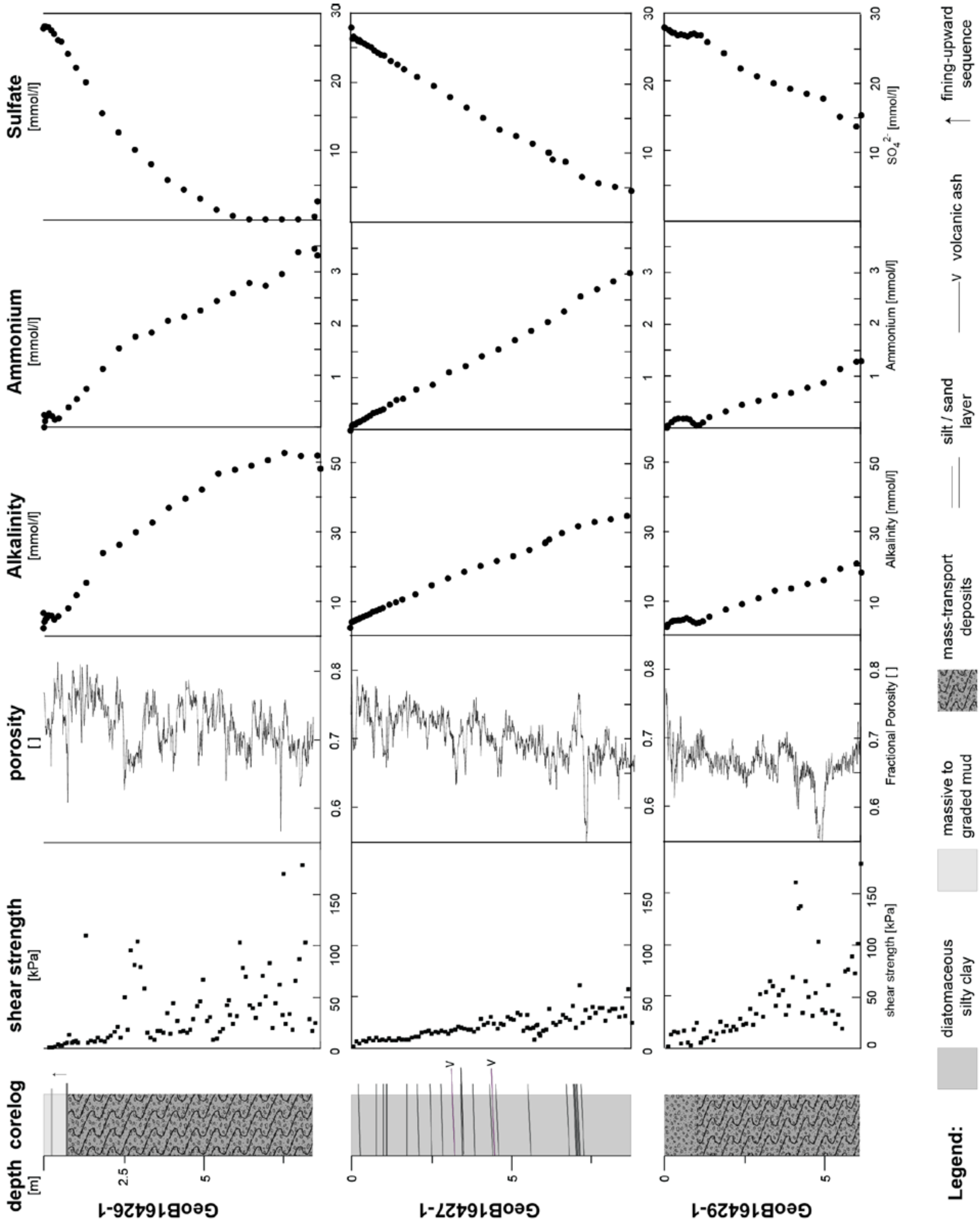

Figure DR1: Physical property and pore-water geochemistry data of cores GeoB16426-1, -27-1 and -29-1:

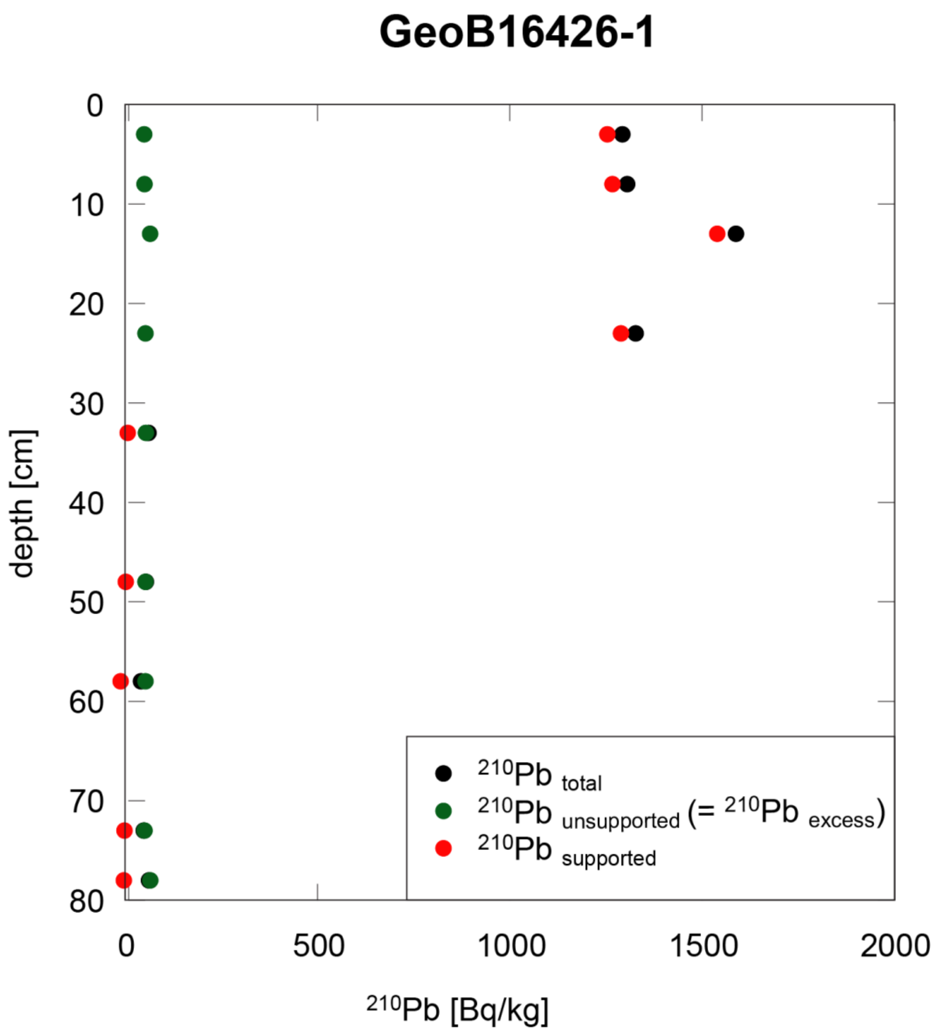

Figure DR2: Results from nondestructive gamma spectrometry showing total, supported and unsupported ^{210}Pb activity measured for the uppermost 80 cm at site GeoB16426-1. Error bars of analytical measurements are smaller than the symbol size.

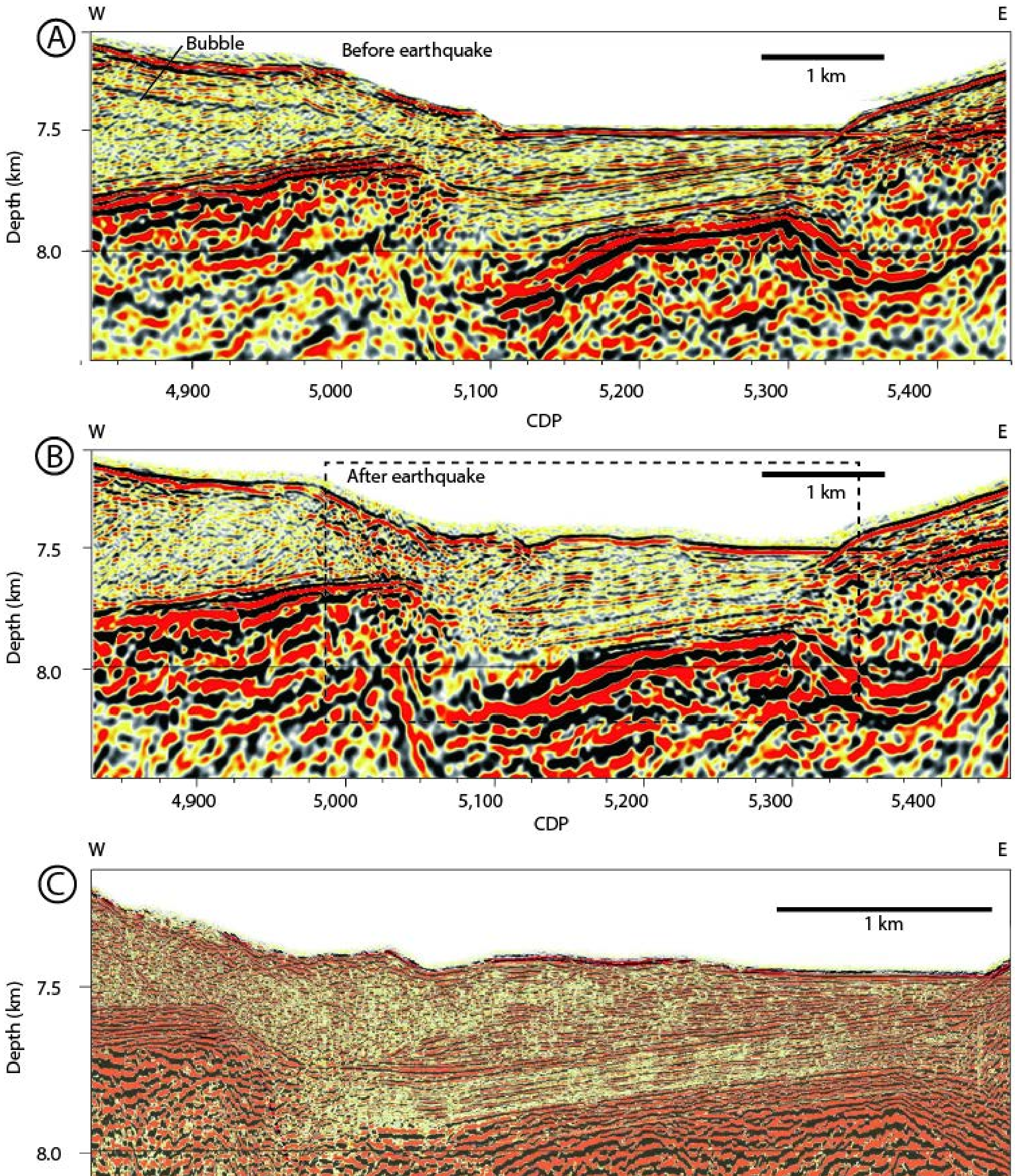

Figure DR3: Comparison of seismic images obtained before and after the earthquake, reproduced from Kodaira et al., (2012; Their figure 4a, 4b and S4a). **A.** Seismic image of the trench axis obtained in 1999 before the earthquake. An interface imaged ~200 m below the seafloor (black interface) at the landward slope of the trench is an artifact generated by a bubble signal from a non-tuned large airgun. Vertical exaggeration, 2:1. **B** Seismic image of the trench axis obtained after the earthquake. Vertical exaggeration, 2:1. **C.** High-resolution seismic image obtained after the earthquake around the trench (within the rectangle shown in Fig S3b)

AUTHOR CONTRIBUTIONS

G.W. and M.S. designed the project and coring survey onboard *R/V Sonne*. T.K. led the coring and analyses during cruise MR12-EO1. C.dSF., T.F. and K.S. contributed bathymetry and seismic data. M.S., M.K., C.dSF., H.F., K.I., K.K., and M.R., acquired and interpreted *R/V Sonne* data. H.F. and S.H. prepared and interpreted gamma spectrometry data. M.S. and M.K. integrated the geological and geochemical data and wrote the paper. All authors equally contributed to scientific discussions.

Marine Geologists SO219A and MR12-E01 science party members contributed to data acquisition and publication within moratorium periods of the cruises.

SO219A marine geologists

Dinten, Dominik,	ETH Zurich, Switzerland
Geprägs, Patrizia,	MARUM, University of Bremen, Germany
Ishitsuka, Kazuya,	Kyoto University, Japan
Kioka, Arata,	AORI, University of Tokyo, Japan
Marcon, Yann	MARUM, University of Bremen, Germany
Podszun, Lina	MARUM, University of Bremen, Germany
Sato, Takeshi,	JAMSTEC, Japan

JAMSTEC Cruise MR12-E01, marine geologists

Arai, Kazuno ,	Chiba University, Japan
Kasaya, Takafumi,	JAMSTEC, Japan
Sato,Tomoyuki ,	AIST, Geological Survey Japan

CITED REFERENCES

Blum, P., 1997, Physical Properties Handbook: A guide to the shopboard measurment of physical porperties of dee-sea cores: ODP Technical Notes, v. 26.

Grasshoff, K., Erhardt, M., and Kremling, 1983, Methods of Seawater Analysis: Weinheim, Verlag Chemie, p. 108-113.

Hall, P. O. J., and Aller, R. C., 1992, Rapid small-volume flow-injection analysis for CO2 and NH4 in marine Sediments: Limnology and Oceanography, v. 35, p. 1113-1119.

Seeberg-Elverfeldt, J., Schlüter, M., Feseker, T., and Kölling, M., 2005, Rhizon sampling of pore waters near the sediment/water interface of aquatic systems: Limnology and oceanography: Methods, v. 3, p. 361-371.

Wood, D. M., 1985, Some fall-cone tests: Géotechnique, v. 38, p. 64-68.